Diese Arbeit wurde vorgelegt am Aerodynamischen Institut

Investigations on two-way coupling effects of particle-laden decaying isotropic turbulent flows

PROJEKTARBEIT

VON

JULIAN STEMMERMANN, STEFFEN TRIENEKENS
UND CHRISTIAN SOIKA

Aerodynamisches Institut der RWTH Aachen

DATUM EINFUEGEN

Betreuer: Konstantin Fröhlich
Erstprüfer: Univ.-Prof. Dr.-Ing. Wolfgang Schröder

Contents

I Nomenclature

Acronyms

CPP	computational point particles
DNS	direct numerical simulation
ILES	implicit large-eddy simulation
LES	large-eddy simulation
PP	particle-laden simulation
rms	root mean square
sgs	subgrid scale
sP	single-phase simulation

Greek Symbols

Δ	cell length
ϵ	viscous dissipation rate
ε	integral dissipation rate
ε'	integral particle induced dissipation rate
$\bar{\varepsilon}$	integral dissipation rate of the background flow field
γ	isentropic exponent
η	Kolmogorov length scale
η_0	initial Kolmogorov length scale
μ	dynamic viscosity
λ_{c}	ratio of physical point particles to computational point particles
ν	kinematic viscosity
ϕ_{m}	mass fraction
ϕ_{v}	volume fraction
Ψ	integral coupling rate
Ψ_{p}	coupling rate for one particle
Ψ_{pp}	integral coupling rate using the point-particle approach
ρ	fluid density
ρ_{p}	particle density
σ	smoothing parameter
$\bar{\boldsymbol{\tau}}$	stress tensor
τ_{η}	Kolmogorov time scale
τ_{L}	eddy turnover time
τ_{p}	particle response time
$\phi(\mathrm{Re_p})$	empirical drag correction factor as a function of the particle Reynolds number Re_{p}
$\boldsymbol{\omega}_{\mathrm{p}}$	particle angular velocity vector

Υ_{f}	fluid domain without particle surroundings

Operators

$\frac{\mathrm{D}}{\mathrm{D}t}$	time derivative following a fluid unit
$\frac{\mathrm{d}}{\mathrm{d}t}$	material derivative
δt	time step
$\frac{\partial}{\partial t}$	partial derivative with respect to time
$\boldsymbol{\nabla}$	nabla operator
:	inner tensor product

Roman Symbols

A	control surface
$\boldsymbol{a}_{\mathrm{p}}$	particle acceleration
c_{p}	specific isobaric heat capacity
c_{v}	specific isochoric heat capacity
d_{i}	distance between particle position and cell center
d_{p}	particle diameter
E	specific inner energy
e	specific internal energy
E_{k}	turbulent kinetic energy of the fluid
E_{kB}	mean kinetic energy of the particles
$\boldsymbol{F}$	force vector per unit volume of the particle acting on the fluid
$\boldsymbol{F}_{\mathrm{p}}$	force vector acting on the particles
$\boldsymbol{F}_{\mathrm{pp}}$	force vector acting on the point-particles
$G(r)$	homogeneous filter function
$\bar{\boldsymbol{H}}$	flux tensor
$\bar{\boldsymbol{H}}^{\mathrm{i}}$	inviscid part of the flux tensor
$\bar{\boldsymbol{H}}^{\mathrm{v}}$	viscous part of the flux tensor
$\bar{\boldsymbol{I}}$	identity tensor
$K(t)$	history kernel
k_{t}	thermal conductivity
L	integral length scale
m_{f}	fluid mass
m_{p}	particle mass
$\boldsymbol{n}$	normal vector
N	grid refinement of the simulation
N_{c}	number of computational point particles
N_{p}	number of physical point particles
p	pressure
Pr	Prandtl number

$\boldsymbol{Q}$	vector of conservative Eulerian variables
$\boldsymbol{q}$	heat conduction vector
R	specific gas constant
$R(r,t)$	two-point correlation as a function of the distance r and time t
Re	Reynolds number
Re_{p}	particle Reynolds number
$\bar{\boldsymbol{S}}$	rate-of-strain tensor
S	Sutherland temperature
T	temperature
t	time
t^*	time normalized by initial eddy turnover time
$\boldsymbol{T}_{\mathrm{p}}$	particle torque vector
$\boldsymbol{u}$	fluid velocity vector
U	characteristic fluid velocity
$\boldsymbol{u}'$	vector of fluid velocity fluctuations
$\boldsymbol{u}_{\mathrm{p}}$	vector of the undisturbed fluid velocity at the particle position
$\bar{\boldsymbol{U}}(\boldsymbol{x})$	filtered velocity field
V	control volume
$\mathrm{V_f}$	fluid volume
$\mathrm{V_p}$	particle volume
$\boldsymbol{v}_{\mathrm{p}}$	particle velocity vector
$\boldsymbol{x}$	position vector
$\boldsymbol{x}_{\mathrm{p}}$	particle position vector

Subscripts

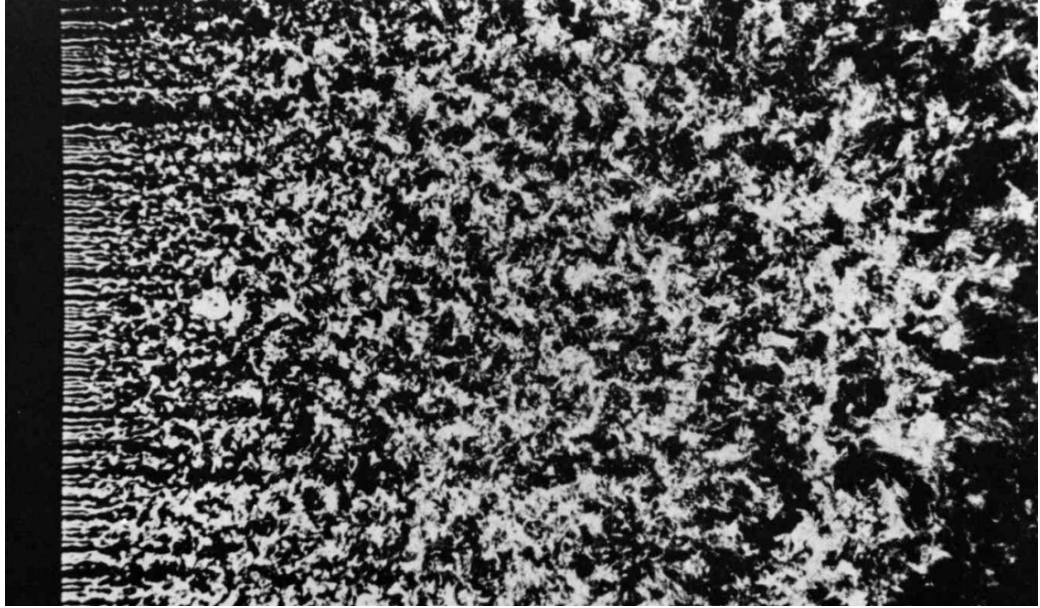|	
∞	freestream value
n	variable at n-th timestep
$n+1$	variable at (n+1)-th timestep
ref	reference value
0	initial values of the variable

1 Introduction

Figure 1: Formation of a locally homogeneuos turbulent flow field behind a grid [6]. An isotropic decaying turbulence can be observed in a snapshot of the flow field moving with the mean flow.

Particle-laden turbulent flows are ubiquitous in nature. Spray automization in fuel injectors, cyclonic particle separation in oil refineries, and sediment accumulation in pipelines are examples for technical applications, where it is of huge interest to predict the impact of the particles on turbulent flows. Turbulence augmentation or attenuation by particles is therefore a decisive factor.

A study about the impact of particles on the isotropic decaying turbulent flow is presented. Incompressible, isothermal, and isotropic decaying turbulence will serve as the carrier flow. Gravity is omitted to avoid prominent directions. Isotropic turbulence is a relatively good assumption of a small region with a high Reynolds number, which is not affected by boundary effects [9]. This concept is visualized in Fig 1. Describing turbulent flows is a difficult task because of the presence of many different scales.

In this work the influence of the particles on the isotropic decaying turbulence is numerically analyzed by using direct numerical simulation (DNS) and large-eddy simulation (LES). DNS are able to resolve all scales of turbulent motion due to their high resolution. LES have a lower grid resolution and use therefore a subgrid-scale model (sgs) for these scales. This type of simulation requires therefore less computational effort.

The simulations were carried out using the point-particle model, where each par-

ticle is tracked via a Langrangian approach. The feedback of the particles on the flow field is modeled by sources and sinks, which is referred to as two-way coupling. Alternatives are one-way coupling, at which only the flow exerts influence on the particles, and four-way coupling, which extends two-way coupling by particle-particle interactions. Two-way coupling is fitting for the simulations in this study, because the volume fraction $\phi_v = 10^{-3}$ of the particles is large enough to alter the turbulence. Volume fractions below $\phi_v = 10^{-6}$ are referred to as one-way coupling and the interactions that can be observed at values greater than $\phi_v = 10^{-3}$ are attributed to four-way coupling [15, 16]. The particle diameter is defined to be smaller than the Kolmogorov scale, i.e., the smallest scale of the turbulent flow. The particle density is much higher than the fluid density.

To lower the computational effort in general, a new variable, which describes the fraction of physical to numerical point particles, is introduced and validated.

In the following, the structure of this work is described. First, mathematical models for single-phase flows and particle dynamics are given. Additionally, the scales of turbulent motion are introduced. Subsequently, the used discretization method to integrate the particle tracking equations is described and the 'computational point particles', in the following referred to as CPP, are introduced. Thereafter, the computational basics of both DNS and LES and their respective advantages and disadvantages are explained. The CPP approach is validated via turbulent kinetic energy budgets for LES and DNS. Finally, a short conclusion is given.

2   Mathematical models

In this section the Navier-Stokes equations in integral formulation, the characteristic turbulent scales and the kinematic and dynamic equations for the particle phase are introduced.

2.1   Equations governing the fluid phase

The conservation of mass, momentum and energy for a control volume V reads

$$\int_V \frac{\partial \boldsymbol{Q}}{\partial t}\,\mathrm{d}V + \int_{\partial V} \bar{\boldsymbol{H}} \cdot \boldsymbol{n}\,\mathrm{d}A = \boldsymbol{0} \tag{2.1}$$

with time t and the flux tensor $\bar{\boldsymbol{H}}$. The vector $\boldsymbol{Q}$ contains the variables fluid density ρ, fluid velocity $\boldsymbol{u}$ and specific inner energy E:

$$\boldsymbol{Q} = \begin{pmatrix} \rho \\ \rho \boldsymbol{u} \\ \rho E \end{pmatrix}. \tag{2.2}$$

$\bar{\boldsymbol{H}}$ is the flux tensor which contains the inviscid and viscous flux, i.e.

$$\bar{\boldsymbol{H}} = \bar{\boldsymbol{H}}^{\mathbf{i}} + \bar{\boldsymbol{H}}^{\mathbf{v}} = \begin{pmatrix} \rho \boldsymbol{u} \\ \rho \boldsymbol{u}\boldsymbol{u} + p \\ \boldsymbol{u}(\rho E + p) \end{pmatrix} - \frac{1}{Re}\begin{pmatrix} 0 \\ \bar{\boldsymbol{\tau}} \\ \bar{\boldsymbol{\tau}}\boldsymbol{u} + \boldsymbol{q} \end{pmatrix}, \tag{2.3}$$

with the shear stress $\bar{\boldsymbol{\tau}}$, heat conduction $\boldsymbol{q}$ and the pressure p. The Reynolds number $Re = \frac{\rho_\infty u_\infty l_{\mathrm{ref}}}{\mu_\infty}$ is defined to be the ratio of inertia forces to viscous forces with reference density ρ_∞, velocity u_∞, length l_{ref} and dynamic viscosity μ_∞. The specific inner energy E and the heat conduction $\boldsymbol{q}$ are defined as

$$E = e\frac{1}{2}|\boldsymbol{u}|^2 \text{ and} \tag{2.4}$$

$$\boldsymbol{q} = -\frac{\mu}{Pr(\gamma - 1)}\boldsymbol{\nabla}T, \tag{2.5}$$

with the constant capacity ratio $\gamma = \frac{c_p}{c_v}$ and the Prandtl number $Pr = \frac{\mu_\infty c_{\mathrm{p}}}{k_{\mathrm{t}}}$ using the specific heat capacities of the fluid c_{v} and c_{p} and thermal conductivity k_{t}. Assuming that the fluid is newtonian, the Stokes hypothesis yields

$$\bar{\boldsymbol{\tau}} = 2\mu\bar{\boldsymbol{S}} - \frac{2}{3}\mu(\boldsymbol{\nabla} \cdot \boldsymbol{u})\bar{\boldsymbol{I}}, \tag{2.6}$$

in which $\bar{\boldsymbol{S}} = \frac{(\boldsymbol{\nabla}\boldsymbol{u})(\boldsymbol{\nabla}\boldsymbol{u})^T}{2}$ denotes the rate-of-strain tensor. Additionally, the viscosity μ can be approximated by Sutherland's law

$$\mu(T) = \mu_\infty \left(\frac{T}{T_\infty}\right)^{3/2}\frac{T_\infty + S}{T + S}, \tag{2.7}$$

where S is the Sutherland temperature. To achieve closure the caloric state equation $e = c_\mathrm{v} T$ and the state equation for an ideal gas $p = \rho R T$ are used. The specific gas constant is determined by $R = c_\mathrm{p} - c_\mathrm{v}$.

2.2 Scales of turbulent flows

Turbulent flows can be described as a superposition of chaotic, three-dimensional vortical structures of various scales, referred to as eddies. Larger eddies decay and pass their kinetic energy down to smaller scales. At the smallest scales, the kinetic energy finally dissipates into heat due to the viscous dissipation. This behavior is called the 'energy cascade' and was first described by Richardson [11] and quantified by Kolmogorov [9].

Considering homogeneous isotropic turbulence, with zero mean velocity and the integral dissipation rate ε, the characteristic length scales of a turbulent flow can be defined by the two-point correlation R, which is the normalized product of the velocity's fluctuation u' at two different positions $\boldsymbol{x}$ and $\boldsymbol{x} + \boldsymbol{e}r$ at the same time t

$$R(r,t) = \frac{\overline{u'(\boldsymbol{x},t)u'(\boldsymbol{x}+\boldsymbol{e}r,t)}}{\overline{u'^2}}, \tag{2.8}$$

as

$$\frac{1}{\lambda^2} = -\frac{1}{2}\left(\frac{\partial^2 R}{\partial r^2}\Big|_{r=0}\right), \tag{2.9}$$

$$\lambda = \sqrt{15\frac{\nu}{\varepsilon}u'} \tag{2.10}$$

or

$$L = \int_0^\infty R(r,t)\,\mathrm{d}r \tag{2.11}$$

with λ being the Taylor microscale, L the integral length scale, u' denoting the absolute value of the velocity's fluctuation and $\boldsymbol{e}$ pointing in the same direction as $\boldsymbol{u'}$ with $|\boldsymbol{e}| = 1$.

The Taylor microscale can be used to compute the Taylor-scale Reynolds number

$$Re_\lambda = \frac{u'\lambda}{\nu}. \tag{2.12}$$

L and the corresponding timescale τ_L, which is mostly called 'eddy turnover time', describe the large eddies. At these scales the energy is brought into the flow, creating the 'energy-containing range'. The eddy turnover time is defined by

$$\tau_\mathrm{L} = \frac{L}{U}, \tag{2.13}$$

4

with the characteristic fluid velocity U.

The smallest scales in a turbulent flow are the Kolmogorov length η and time scale τ_η. At these scales, the effects of viscosity take place and the energy dissipates into heat. With the estimate $\varepsilon \approx \frac{U^3}{L}$ they can be written as

$$\eta = \left(\frac{\nu^3 L}{U^3} \right)^{1/4} \tag{2.14}$$

and

$$\tau_\eta = \left(\frac{\nu L}{U^3} \right). \tag{2.15}$$

Both these scales are coupled by the Reynolds numbers

$$\frac{L}{\eta} = Re^{3/4} \tag{2.16}$$

and

$$\frac{\tau_\mathrm{L}}{\tau_\eta} = Re_\mathrm{L}^{1/2} \tag{2.17}$$

with $Re_\mathrm{L} = \frac{u'L}{\nu}$. It can be observed from these equations that the spacing between the scales increases for higher Reynolds numbers.

2.3 Particle dynamics

$\boldsymbol{F}_\mathrm{pp}$ is the sum of several pressure and shear forces acting on the particles and is described explicitly by the Maxey-Riley equation [12]. Reduced to the governing forces and with neglection of gravity the dynamic equation of the particles becomes

$$\boldsymbol{F}_\mathrm{pp} = m_\mathrm{p} \frac{\mathrm{d}\boldsymbol{v}_\mathrm{p}}{\mathrm{d}t} = \rho V_\mathrm{p} \frac{\mathrm{D}\boldsymbol{u}_\mathrm{p}}{\mathrm{D}t} + 3\pi \mu d_\mathrm{p} (\boldsymbol{u}_\mathrm{p} - \boldsymbol{v}_\mathrm{p}) \phi(Re_\mathrm{p}) + \frac{1}{2} \rho V_\mathrm{p} \left(\frac{\mathrm{D}\boldsymbol{u}_\mathrm{p}}{\mathrm{D}t} - \frac{\mathrm{d}\boldsymbol{v}_\mathrm{p}}{\mathrm{d}t} \right) +$$
$$3\pi \mu d_\mathrm{p} \int_0^t K(t)(t - t') \cdot \left(\frac{\mathrm{d}\boldsymbol{u}_\mathrm{p}}{\mathrm{d}t'} - \frac{\mathrm{d}\boldsymbol{v}_\mathrm{p}}{\mathrm{d}t'} \right) dt'. \tag{2.18}$$

$\boldsymbol{v}_\mathrm{p}(\boldsymbol{x}_\mathrm{p}, t)$ is the particle velocity vector with the time derivative $\mathrm{d}/\mathrm{d}t$ along the particle trajectory while $\mathrm{D}/\mathrm{D}t$ is the material derivative at one point. $\boldsymbol{u}_\mathrm{p}(t) = \boldsymbol{u}_\mathrm{p}(\boldsymbol{x}_\mathrm{p}, t)$ is the velocity of the undisturbed fluid at the particle position $\boldsymbol{x}_\mathrm{p}$. The individual forces on the right side of the equation are stated in the following:

- $\rho V_\mathrm{p} \frac{\mathrm{D}\boldsymbol{u}_\mathrm{p}}{\mathrm{D}t}$:
  pressure gradient of the undisturbed flow

- $3\pi \mu d_\mathrm{p} (\boldsymbol{u}_\mathrm{p} - \boldsymbol{v}_\mathrm{p}) \phi(Re_\mathrm{p})$:
  quasi-steady Stokes drag that is parallel to the undisturbed streamlines and is described by the Stokes' law as the force of viscosity acting on the interface of small spherical particles and fluid that can be achieved at very low Reynolds numbers in a viscous fluid

- $\frac{1}{2}\rho V_p \left(\frac{Du_p}{Dt} - \frac{dv_p}{dt} \right)$:

  added mass force, representing the influence of the fluid's inertia that has an impact on the particle, in case of a different acceleration than the particles

- $3\pi\mu d_p \int_0^t K(t)(t - t') \cdot \left(\frac{du_p}{dt'} - \frac{dv_p}{dt'} \right) dt'$:

  Basset history force taking the unsteady motion into account using a history kernel $K(t)$

(2.18) is based on Stokes flow conditions, i.e., vanishing particle Reynolds number $Re_p \ll 1$. In addition in this thesis, particles with $d_p \ll \eta$ are investigated. As a result for heavy particles, the drag force is the dominating contributor of Eq. (2.18) as reported by [20]. Therefore $\boldsymbol{F}_{pp}$ can be reduced to

$$\boldsymbol{F}_{pp} = m_p \frac{d\boldsymbol{v}_p}{dt} = 3\pi\mu d_p (\boldsymbol{u}_p - \boldsymbol{v}_p)\phi(Re_p). \tag{2.19}$$

The empirical correction factor $\phi(Re_p) = 1 + 0.15 Re_p^{0.687}$ is used for finite Re_p. Eq. (2.19) can be reformulated to

$$\frac{d\boldsymbol{v}_p}{dt} = \frac{\phi(Re_p)}{\tau_p}(\boldsymbol{u}_p - \boldsymbol{v}_p), \tag{2.20}$$

with the particle relaxation time $\tau_p = \frac{1}{18} \frac{\rho_p}{\rho} \frac{d_p^2}{\nu}$.

Together with the kinematic equation

$$\frac{d\boldsymbol{x}_p}{dt} = \boldsymbol{v}_p, \tag{2.21}$$

the Eqs. (2.1) and (2.19) form a closed system of equations.

3 Numerical methods

Two numerical methods are discussed and their main differences pointed out in the following chapter, the DNS (direct numerical simulation) and the LES (large-eddy simulation). The basis of both are the Navier-Stokes equations as described above. The simulations were carried out using ZFS, the simulation tool developed and implemented at the Institute of Aerodynamics at RWTH Aachen University [4] [5]. The tool is capable of simulating compressible finite-volume flows using unstructured Cartesian grids.

3.1 Discretization of the particle dynamics

To compute the Lagrangian particle trajectories, a predictor-corrector scheme based on the trapezoidal rule for numerical integration

$$f(t + \delta t) \approx f(t) + \frac{\delta t}{2} \left[\frac{\partial f(t)}{\partial t} + \frac{\partial f(t + \delta t)}{\partial t} \right] \tag{3.1}$$

is used.

The first step is the prediction of the new particle position $\boldsymbol{x}_{\mathrm{p},n+1}$ using a Taylor expansion for a small time step δt

$$\boldsymbol{x}_{\mathrm{p},n+1} = \boldsymbol{x}_{\mathrm{p},n} + \delta t \boldsymbol{v}_{\mathrm{p},n} + \frac{1}{2} \delta t^2 \boldsymbol{a}_{\mathrm{p},n}, \tag{3.2}$$

with $\boldsymbol{a}_{\mathrm{p},n}$ particle acceleration, where the subscript p denotes the particle and the subscript n the time step.

To avoid filtering effects, the fluid velocity $\boldsymbol{u}_{\mathrm{p},n+1}$ at the particle position $\boldsymbol{x}_{\mathrm{p},n+1}$ is set equal to the nearest cell fluid velocity.

The predicted velocity and acceleration are calculated with

$$\boldsymbol{v}_{\mathrm{p},n+1} = \frac{\boldsymbol{v}_{\mathrm{p,n}} + \frac{1}{2}\delta t \left(\boldsymbol{a}_{\mathrm{p,n}} + \frac{f_{\mathrm{d}}}{\tau_{\mathrm{p}}} \boldsymbol{u}_{\mathrm{p},n+1} \right)}{1 + \frac{1}{2}\frac{f_{\mathrm{D}}}{\tau_{\mathrm{p}}}\delta t}, \tag{3.3}$$

$$\boldsymbol{a}_{\mathrm{p},n+1} = \frac{\frac{f_{\mathrm{D}}}{\tau_{\mathrm{p}}} \left(\boldsymbol{u}_{\mathrm{p},n+1} - \boldsymbol{v}_{\mathrm{p,n}} - \frac{1}{2}\delta t \boldsymbol{a}_{\mathrm{p},n} \right)}{1 + \frac{1}{2}\frac{f_{\mathrm{D}}}{\tau_{\mathrm{p}}}\delta t}. \tag{3.4}$$

The updated particle position must be corrected by an additional term according to the trapezoidal rule

$$\boldsymbol{x}_{\mathrm{p},n+1} = \boldsymbol{x}_{\mathrm{p},n} + \frac{1}{2}\delta t \left(\boldsymbol{v}_{\mathrm{p},n+1} + \boldsymbol{v}_{\mathrm{p},n} \right) + \frac{1}{12}\delta t^2 \left(\boldsymbol{a}_{\mathrm{p},n+1} - \boldsymbol{a}_{\mathrm{p},n} \right). \tag{3.5}$$

These approaches to compute the particle trajectories require a lot of computational resources.

Due to reduce this requirement the creation of numerical clusters of point particles is considered. For this purpose the ratio λ_c of physical point particles N_p to CPPs N_c is introduced ($\lambda_c = \frac{N_p}{N_c}$). To compensate this lack of particles, the feedback force is multiplied by λ_c, due to the λ_c-fold mass of the (cluster-)particles.

To model the impact of the particles on the fluid, the Navier-Stokes equations (2.1) are extended by momentum sources or sinks. The feedback force of the particles is exerted on the fluid using a distance based weighting function

$$\boldsymbol{F} = \boldsymbol{F}_{\mathrm{pp}} \cdot \frac{\mathrm{e}^{-\left(d_i^2/(\sigma \Delta^2)\right)}}{\sum\limits_{i} e^{-\left(d_i^2/(\sigma \Delta^2)\right)}}, \tag{3.6}$$

with the distance between particle postion and the cell center d_i, the grid width Δ, and a smoothing parameter σ that controls the distribution of $\boldsymbol{F}$ on the adjacent cells.

3.2 Direct numerical simulation

With DNS, the Navier-Stokes equations are solved completely. This provides a very accurate result, as all scales of motion are being resolved. Hence it requires an immense level of computational resources which increases rapidly with the Reynolds number: $N \propto Re_\lambda^{9/2}$ with the gridsize N of the simulation. With the LES, as described below, the computational effort is 99.98 % less compared to DNS, which is the fraction of the dissipative scale. This leaves 0.02 % of the flow, which is correlative with the fraction of the energy-containing larger-scale [14].

3.3 Large-eddy simulation

Due to the fact that DNS is effortful, LES was created to save time and resources. The energy containing large scales are completely resolved and the impact of the small scales on the large scales are modeled.

Simulating only the larger-scale motions is called filtering, which means that the smaller-scale motions, also known as fluctuation, are filtered out. The filtered velocity field is calculated by

$$\bar{U}(\boldsymbol{x}) = \int_{-\infty}^{\infty} G(\boldsymbol{r}) U(\boldsymbol{x} - \boldsymbol{r}) \, \mathrm{d}\boldsymbol{r}, \tag{3.7}$$

with $G(\boldsymbol{r})$ being a homogeneous filter function [14]. To model the filtered smaller-scale motions a subgrid-scale (sgs) model is necessary. According to Hickel (2007)
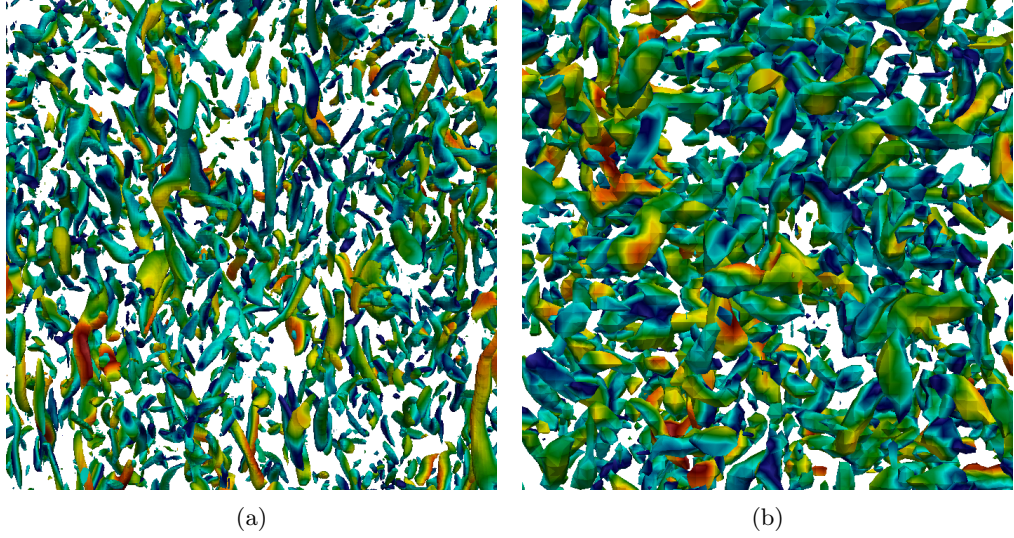
Figure 2: Instantaneous snapshot of the parallel projection of an isotropic decaying turbulent flow field computed by a DNS (a) and an LES_{64} (b). 'Worm-like' structures in an isotropic turbulent flow field. The more refined grid on the left shows more and better resolved structures, while the right picture reveals more artificially generated artifacts. For details on creation, see Appendix.

the interference between explicit sgs and the truncation error can be exploited, i.e. the truncation error can serve as model of the effects of unresolved scales, which is therefore an implicit sgs model. Thus it is called implicit LES (ILES) [18]. Even though the small scales are modeled in the LES, the effects of filtering can be seen in figure 2.

4 Results

In this section, the setup and the results of the DNS and LES of particle-laden decaying isotropic turbulence will be presented. Special emphasis will be put on the turbulent kinetic energy budgets and their use to interpret the results.

4.1 Turbulence modulation by particles

The particle-laden turbulence modulation by particles in decaying isotropic turbulence is determined by the coupling rate Ψ, which describes the energy transfer between the fluid and the particle phase, the background dissipation rate of the flow field $\bar{\varepsilon}$ and the particle-induced dissipation rate ε'. These contributions form an equation, which describes the change in turbulent kinetic energy

$$\frac{\mathrm{d}E_{\mathrm{k}}}{\mathrm{d}t} = \Psi(t) - \bar{\varepsilon}(t) - \varepsilon'(t). \tag{4.1}$$

As the dissipation rate is always of positive value, it acts as a sink for the turbulent kinetic energy. In contrast to that, the coupling rate can serve either as source or sink depending on the acceleration of the particles [10]. The coupling rate for fully resolved particles Ψ is defined as

$$\Psi(t) = \sum_{p=1}^{N_{\mathrm{p}}} \Psi_{\mathrm{p}} = -\sum_{p=1}^{N_{\mathrm{p}}} (\boldsymbol{F}_{\mathrm{p}} \cdot \boldsymbol{v}_{\mathrm{p}} + \boldsymbol{T}_{\mathrm{p}} \cdot \boldsymbol{\omega}_{\mathrm{p}}), \tag{4.2}$$

using surface force $\boldsymbol{F}_{\mathrm{p}}$, particle velocity $\boldsymbol{v}_{\mathrm{p}}$, torque $\boldsymbol{T}_{\mathrm{p}}$ and angular velocity $\boldsymbol{\omega}_{\mathrm{p}}$ to describe the transfer of kinetic energy resulting at each particle.

As mentioned before, the flow field is considered nearly incompressible, therefore the equation for the viscous dissipation rate can be approximated by

$$\epsilon(t) \approx 2\mu \bar{\boldsymbol{S}} : \bar{\boldsymbol{S}}, \tag{4.3}$$

where $:$ denotes the inner tensor product. This rate can then be integrated over the fluid domain excluding particles and their direct surroundings Υ_{f}, which leads to the background dissipation rate

$$\bar{\varepsilon}(t) = \int_{\Upsilon_{\mathrm{f}}} \epsilon(t)\mathrm{d}V. \tag{4.4}$$

Additionally, the particles change the fluid's rate of dissipation due to their volume forces. Neglecting fluid inertia forces, the additional dissipation rate for fully resolved particles can be computed by

$$\varepsilon' = \sum_{p=1}^{N_{\mathrm{p}}} \boldsymbol{F}_{\mathrm{p}} \cdot (\boldsymbol{u}_{\mathrm{p}} - \boldsymbol{v}_{\mathrm{p}}) + \boldsymbol{T}_{\mathrm{p}} \cdot (\boldsymbol{\Omega}_{\mathrm{p}} - \boldsymbol{\omega}_{\mathrm{p}}),\ \rho_{\mathrm{p}} \gg \rho, \tag{4.5}$$

using the vorticity vector of the undisturbed flow around one particle $\mathbf{\Omega}_\mathrm{p}$ at the particle position.

For $\rho_\mathrm{p} \gg \rho$, and the point-particle approach the coupling rate Ψ and the additional dissipation rate ε' are implicitly coupled. Torque and angular velocity were neglected for the point-particle approach and F_pp is modeled with Eq. 2.19, which leads to

$$\Psi_\mathrm{pp}(t) = \Psi - \varepsilon'(t) = -\sum_{p=1}^{N_\mathrm{p}} \boldsymbol{F}_\mathrm{pp} \cdot \boldsymbol{u}_\mathrm{p}. \tag{4.6}$$

Therefore, the turbulent kinetic energy budget for the point-particle approach reads

$$\frac{\mathrm{d}E_\mathrm{k}}{\mathrm{d}t} = \Psi_\mathrm{pp}(t) - \bar{\varepsilon}(t) = -\sum_{p=1}^{N_\mathrm{p}} \boldsymbol{F}_\mathrm{pp} \cdot \boldsymbol{u}_\mathrm{p} - \bar{\varepsilon}(t). \tag{4.7}$$

4.2 Simulation setup

All cases were simulated on a cubic domain and a Cartesian grid using different grid refinement levels. For the LES cases 64^3, 96^3 and 128^3 cells are employed, which have been already validated in [8]. For a DNS, 256^3 cells are necessary to resolve all scales.

The particle-free case was initialized using a seed-based random number generator, which is described in detail in [19]. At $t^* = t\frac{\varepsilon_0}{u_0{}^2} \approx 0.27 = t_\mathrm{inj}^*$, where t^* is the time normalized by the initial viscous dissipation rate ε_0 and initial rms-velocity u_0, a restart file is written out to initialize the subsequent simulation of the particle-laden isotropic turbulence.

The single-phase DNS and particle-laden DNS will be used as reference for analyzing other results. The single-phase results will be in the following referred to as sP, and particle-laden results as PP. The PP simulations are set up to match the volume fraction $\phi_\mathrm{v} = \frac{V_\mathrm{p}}{V_\mathrm{f}} = 10^{-3}$ and mass fraction of $\phi_\mathrm{m} = \frac{m_\mathrm{p}}{m_\mathrm{f}} = 1$. Hence, the density ratio is $\frac{\rho_\mathrm{p}}{\rho} = 1000$ and the particle diameter is $d_\mathrm{p} \approx 0.6\eta_0$ with η_0 being the initial Kolmogorov length. At the time step of the injection, the Taylor Reynolds number is $Re_\lambda \approx 58$.

4.3 Simulation results

At first, a test is required to investigate the number of particles needed to achieve approximately converged statistics.

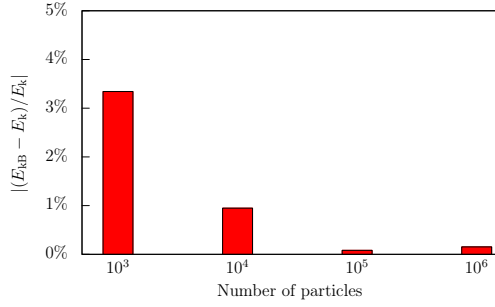Figure 3 therefore shows the relative deviation of the particles' kinetic energy E_kB

Figure 3: Relative deviation of the kinetic energy of the particles E_{kB} from the turbulent kinetic energy E_k at t_{inj}^* for an LES_{128}. An inaccuracy can be observed for small numbers of particles. This behavior can be noticed for all other resolutions. Relative deviation of the particles' kinetic energy and the turbulent kinetic energy is below 1% for 10^4 particles.
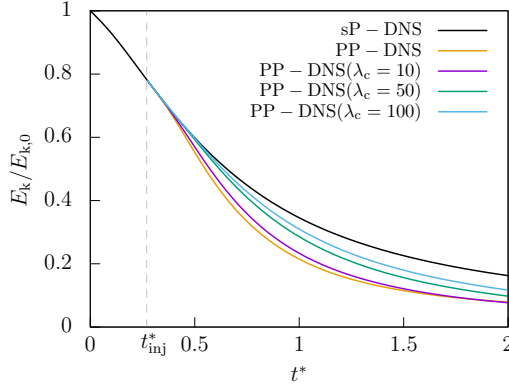

Figure 4: Temporal development with time normalized by initial eddy turnover time t^* of the kinetic energy E_k normalized by its initial value $E_{k,0}$. Shortly after the injection, the PP-cases separate from the sP-flow. The higher-clustered cases show significant differences compared to the reference case PP-DNS.
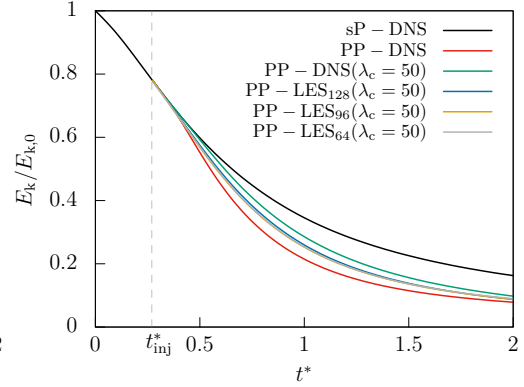
Figure 5: Temporal development of the kinetic energy E_k normalized by its initial value $E_{k,0}$ for different grid resolutions and with constant $\lambda_c = 50$. The lower-resolution simulation results are more similar to the particle-laden reference case PP-DNS.

from the turbulent kinetic energy E_k at injection time for different numbers of particles. For higher numbers of particles the deviation subsides. For 10^4 particles the deviation is below 1%. This leads to the assumption that simulations with a λ_c of 100 seem fitting with an overall number of a million particles.

To investigate the influence of CPPs on the accuracy of the simulations, the variable λ_c, introduced in Sec. 3.1, was implemented in the program code. All simulations were then set up with the overall same number of a million particles, and λ_c was set to 10, 50 and 100. Additionally, simulations of the single-phase flow and an unclustered particle-laden flow were conducted. A DNS serves as reference for later evaluations.

Figure 4 shows the evolution of the turbulent kinetic energy E_k normalized by the initial turbulent kinetic Energy $E_{k,0}$ in time of the DNS using different λ_c and
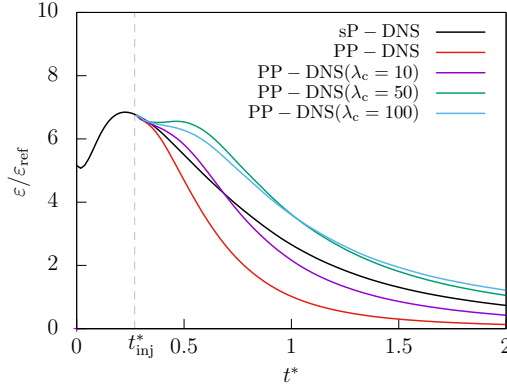
12

Figure 6: Temporal development of the normalized dissipation rate $\bar{\varepsilon}$. The unclustered PP-case shows a lower dissipation rate than the sP-case. Highly clustered PP-cases show a higher dissipation rate.
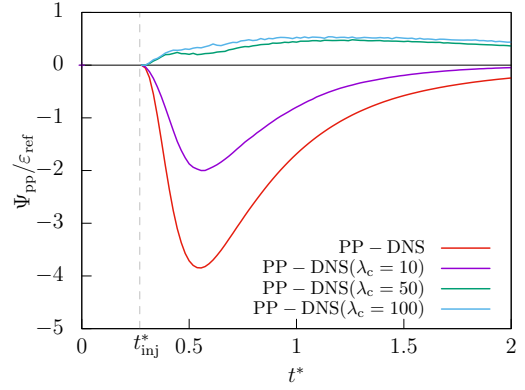
Figure 7: Temporal development of the normalized point-particle coupling rate Ψ_{pp}. The PP-case without clustering shows the lowest coupling rate. Both highly-clustered PP-cases show positive contribution in contrast to the reference case PP-DNS.

constant grid resolution. Shortly after injection, the number of clustered particles has a high impact on the turbulent kinetic energy. For increasing λ_{c}, the turbulence attenuation by particles is underpredicted.

The behavior of lower-resolution particle-laden simulations seems to be less prone to CPPs, as it can be seen in Fig. 5. The same variables are displayed as in Fig. 4, this time for constant $\lambda_{\mathrm{c}} = 100$ using different grid resolutions. The coarser simulations are closer to the PP-DNS reference as the high-resolution simulations. It can be seen that both the CPPs and the grid refinement level have an influence on the simulation's accuracy. Therefore further investigations on the reasons of this behavior will follow.

The development of the normalized dissipation rate $\bar{\varepsilon}$ is displayed in Fig. 6, showing a lower rate for the unclustered PP-DNS and a higher rate for the higher-clustered DNS cases in comparison to the single-phase simulation. The dissipation rate is therefore normalized by its reference value $\varepsilon_{\mathrm{ref}} = \frac{u_0^3}{L}$.

Figure 7 displays the evolution in time of the point-particle coupling rate Ψ_{pp}. Similar to Fig. 6, the DNS with high CPP show larger deviation from the PP-DNS reference, leading to a positive coupling rate for $\lambda_{\mathrm{c}} \gg 50$.

Bot these figures can be analyzed using the turbulent kinetic energy budget introduced in Sec. 4.1. The variables of the DNS and LES_{64} at $t^* = 1$ can be found in Tab.1. A general trend for less accurate results can be observed for higher mass ratios of one particle cluster to the content of one cell. As the LES_{64} is not fine enough to resolve the smaller scales, the first three values are not displayed in the table. The simulation on a 64^3-grid is therefore less susceptible to altering the

Case	λ_c	$\frac{m_c}{m_{V,cell}}$	$\varepsilon\frac{L}{u_0{}^3}$	$\frac{\lambda}{L}$	$\frac{\eta}{L}$	Re_λ	$E_k/E_{k,0}$	$E_{kB}/E_{k,0}$
DNS	1	16.78	0.97	0.039	0.0032	38.73	0.21	0.29
	10	167.78	2.08	0.028	0.0026	28.66	0.23	0.34
	50	838.86	3.51	0.024	0.0023	27.31	0.28	0.52
	100	1677.72	3.51	0.025	0.0023	29.42	0.31	0.62
LES$_{64}$	1	0.26				48.26	0.23	0.28
	10	2.62				48.13	0.23	0.28
	50	13.11				47.54	0.25	0.30
	100	26.21				47.60	0.27	0.30

Table 1: Variables of the simulations at $t^* = 1$ of the PP-DNS and the PP $-$ LES$_{64}$.
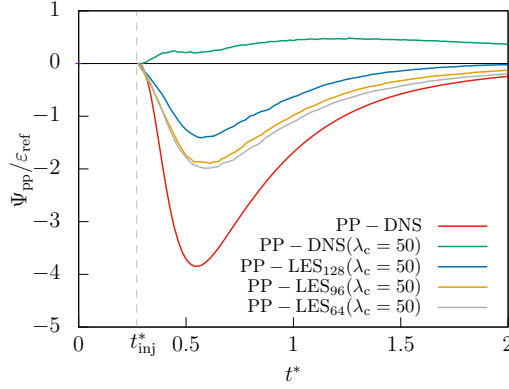

Figure 8: Temporal development of the point-particle coupling rate Ψ_{pp} with constant λ_c for various resolutions. A relation of resolution and accuracy can be observed.
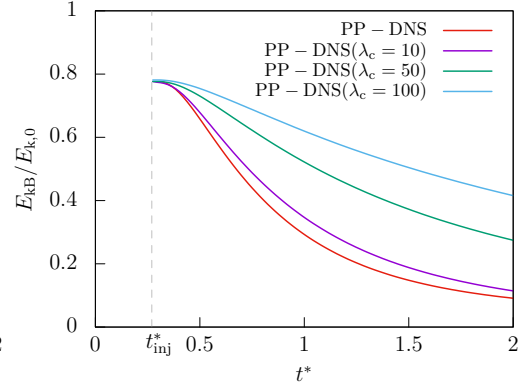

Figure 9: Temporal development of the kinetic energy of the particles E_{kB} normalized by initial turbulent kinetic energy. The PP-case without clustering shows the biggest decay in kinetic energy.

14

CPPs because the cells, and therefore the mass of one cell, are substantially bigger than in the 256^3-grid for a constant domain size. It seems to be the case that for increasing mass ratio of one cluster to one cell the simulation results become less accurate. This phenomenon was first described in [13], as particle-induced point forces induce a vorticity to the flow at the particle position.

Although this mass ratio is relatively big for the PP-DNS, this simulation delivers the best results. Higher grid refinement leads to better results, while higher mass fractions of particles to cells lead to less accurate results. The assumption that for the PP-DNS both these effects form the best compromise therefore is natural. Figure 8 can be used to point out the difference in susceptibility for this method. The evolution of the point-particle coupling rate Ψ_{pp} for different grid refinement levels is displayed. It is evident that a correlation between inaccuracy of the simulations and the refinement level of the grid exists. For the same ratio of physical point particles to CPPs the results show different behavior depending on the grid refinement level. The unclustered PP-case is included as reference. It is therefore less critical to cluster particles in lower-resolution grids, although the results are not nearly as accurate as for the unclustered simulations.

In Fig. 9, the development of kinetic energy of the particles is displayed. For increasing λ_c, the kinetic energy of the particles becomes larger. This behavior leads to the assumption that the clustering produces the behavior of heavy particles comparable to [10].

All this results arise the question, if and how the method of CPPs could be used to optimize computational effort and still deliver accurate results. Therefore further investigation on this topic is needed.

5 Conclusion and outlook

In this study, multiple simulations were carried out to evaluate a method for lowering computational effort. Multiple simulations of particle-laden isotropic turbulence were carried out to investigate the influence of CPPs on the simulation accuracy of DNS and multiple LES. A point-particle approach was used to simulate the two-way coupling of heavy particles and the surrounding fluid. The particle diameter was smaller than the Kolmogorov scale $d_\infty < \eta$. A DNS on a grid with 256^3 grid point served as reference for validation of the method of CPPs. CPPs were introduced in various numbers on multiple grid refinement levels. The concept of CPPs was object of this study because of the possible potential in lowering computational effort for future simulations. Therefore the accuracy of the simulations was the critical criteria. Several plots were created to analyze possible correlation of different variables and the influence of grid refinement level and CPPs. Besides the evolution of the kinetic energy the point-particle coupling rate and the dissipation rate were evaluated.

A correlation between the mass fraction of one particle cluster to the content of one cell was found. With this fraction increasing, the simulations diverge from the reference case. This behavior was found at all simulations. In difference to that, the reference PP-DNS has a relatively high ratio of masses and is nevertheless the most accurate. In addition to that the results of simulations with lower mass ratios do not necessarily converge towards the reference. It is obvious that the mass ratio is not the only parameter responsible for accurate or inaccurate results. Most probably a combination of grid refinement and mass ratio is responsible for accuracy in the simulations.

It was found that the behavior of particle clusters as simulated in this work shows similarities to heavy particles, as simulated in [10].

The method evaluated in this work seems to be less useful for this particle parameters. The method could be useful for smaller particles, which would have a smaller fraction of mass for the same number of particles simulated. This feature could make the method worthwhile for them. Further investigation regarding this use case and the specific mass fraction and grid refinement combination could be tested in the future to develop a catalog of mass fractions, grid refinement and the resulting accuracy for practical use in technical applications.

6 References

[1] A. Ferrante and S. Elghobashi. On the physical mechanisms of two-way coupling in particle-laden isotropic turbulence. *Phys. Fluids*, 15(2):315–329, 2003.

[2] A. Prosperetti and G. Tryggvason. *Computational methods for multiphase flow*. Cambridge University Press, 2009.

[3] C. Siewert. *Numerical Analysis of Particle Collisions in Isotropic Turbulence*. PhD thesis, 2014.

[4] D. Hartmann, M. Meinke and W. Schröder. An adaptive multilevel multi-grid formulation for Cartesian hierarchical grid methods. *Comput. Fluids*, 37(9):1103–1125, 2008.

[5] D. Hartmann, M. Meinke and W. Schröder. A strictly conservative Cartesian cut-cell method for compressible viscous flows on adaptive grids. *Comput. Methods in Appl. Mech. Eng.*, 200(9):1038–1052, 2011.

[6] Van Dyke. *An album of fluid motion*. Parabolic Press Stanford, 1982.

[7] J.R. Fessler, J.D. Kulick and J.K. Eaton. Preferential concentration of heavy particles in a turbulent channel flow. *Phys. Fluids*, 6(11):3742–3749, 1994.

[8] K. Fröhlich, L. Schneiders, M. Meinke and W. Schröder. Validation of Particle-Laden Large-Eddy Simulation Using HPC Systems. In *Sustained Simulation Performance 2017*, pages 137–149. Springer, 2017.

[9] A. N. Kolmogorov. The local structure of turbulence in incompressible viscous fluid for very large reynolds numbers. *Proc. Royal Soc. A*, 434(1890):9–13, 1991.

[10] L. Schneiders, M. Meinke and W. Schröder. Direct particle–fluid simulation of kolmogorov-length-scale size particles in decaying isotropic turbulence. *J. Fluid Mech.*, 819:188–227, 2017.

[11] L.F. Richardson. The supply of energy from and to atmospheric eddies. *Proc. Royal Soc. A*, 97(686):354–373, 1920.

[12] M.R. Maxey and J.J. Riley. Equation of motion for a small rigid sphere in a nonuniform flow. *Phys. Fluids*, 26(4):883–889, 1983.

[13] M.R. Maxey, B.K. Patel, E.J. Chang and L.-P. Wang. Simulations of dispersed turbulent multiphase flow. *Fluid Dyn. Res.*, 20(1-6):143–156, 1997.

[14] S. B. Pope. *Turbulent flows.* Cambridge University Press, 2000.

[15] S. Elghobashi. Particle-laden turbulent flows: direct simulation and closure models. *Appl. Sci. Res.*, 48(3):301–314, 1991.

[16] S. Elghobashi. On predicting particle-laden turbulent flows. *Appl. Sci. Res.*, 52(4):309–329, 1994.

[17] S. Elghobashi and G.C. Truesdell. Direct simulation of particle dispersion in a decaying isotropic turbulence. *J. Fluid Mech.*, 242:655–700, 1992.

[18] S. Hickel. *Implicit turbulence modeling for large-eddy simulation.* PhD thesis, 2008.

[19] S.A. Orszag. Numerical methods for the simulation of turbulence. *Phys. Fluids*, 12(12):II–250, 1969.

[20] V. Armenio and V. Fiorotto. The importance of the forces acting on particles in turbulent flows. *Phys. Fluids*, 13(8):2437–2440, 2001.

7 Appendix

Creating of pictures showing tubular structures

The pictures used in to point out the differences between DNS and LES were generated using ParaView, an open-source-software developed by a joint-venture of Kitware and the Los Alamos National Laboratory. More information about the software can be found at www.paraview.org. To show the tubular structures in a turbulent flow, two filters were used: One was the AIALambda2Criterion1-Filter and the other one was the ISOVolume1-Filter. These filters were then set to visualize the velocity of the flow colored by magnitude. To diversify the different velocity-magnitudes, a rainbow-colorscheme was used.